


FULL PAPER

Open Access



Magnetic Search Coil (MSC) of Plasma Wave Experiment (PWE) aboard the Arase (ERG) satellite

Mitsunori Ozaki^{1*} , Satoshi Yagitani¹, Yoshiya Kasahara¹, Hirotsugu Kojima², Yasumasa Kasaba³, Atsushi Kumamoto³, Fuminori Tsuchiya³, Shoya Matsuda⁴, Ayako Matsuoka⁵, Takashi Sasaki⁶ and Takahiro Yumoto⁶

Abstract

This paper presents detailed performance values of the Magnetic Search Coil (MSC) that is part of the Plasma Wave Experiment on board the Arase (ERG) satellite. The MSC consists of a three-axis search coil magnetometer with a 200-mm-long magnetic core. The MSC plays a central role in the magnetic field observations, particularly for whistler mode chorus and hiss waves in a few kHz frequency range, which may cause local acceleration and/or rapid loss of radiation belt electrons. Accordingly, the MSC was carefully designed and developed to operate well in harsh radiation environments. To ascertain the wave-normal vectors, polarizations, and refractive indices of the plasma waves in a wide frequency band, the output signals detected by the MSC are fed into the two different wave receivers: one is the WaveForm Capture/Onboard Frequency Analyzer for waveform and spectrum observations in the frequency range from a few Hz up to 20 kHz, and the other is the High Frequency Analyzer for spectrum observations in the frequency range from 10 to 100 kHz. The noise equivalent magnetic induction of the MSC is $20 \text{ fT/Hz}^{1/2}$ at a frequency of 2 kHz, and the null depth of directionality is -40 dB , which is equivalent to an angular error less than 1° . The MSC on board the Arase satellite is the first experiment using a current-sensitive preamplifier for probing the plasma waves in the radiation belts.

Keywords: Search coil magnetometer, Arase (ERG) satellite, Plasma waves, Radiation belts, Geospace

Introduction

Important role of plasma waves in radiation belt dynamics

The radiation belts surrounding the Earth contain enhanced relativistic particles (Baker et al. 1986; Reeves et al. 2003; Miyoshi and Kataoka 2005; Shprits et al. 2013). The inner radiation belt ($L \approx 1$ to 3) is dominated by relativistic protons, while the outer belt ($L \approx 4$ to 6) consists of relativistic electrons trapped in the geomagnetic fields. A third belt is found between geomagnetic storms (Baker et al. 2013). Although the acceleration and loss mechanisms of the radiation belts are still open questions, it has been established that plasma waves fulfill a

crucial role in both processes (Schulz and Lanzerotti 1974; Summers et al. 1998; Thorne 2010). Two major mechanisms have been presented: one is inward and outward radial diffusion via ultralow-frequency (ULF) waves (e.g., Schulz and Lanzerotti 1974; Elkington et al. 1999; Hudson et al. 2000; Shprits et al. 2008), and the other is local acceleration and loss processes via wave-particle interactions (e.g., Summers et al. 1998; Thorne 2010; Thorne et al. 2013). It is particularly noteworthy that the Van Allen Probes have observed local electron acceleration during a geomagnetic storm (Reeves et al. 2013), which tends to support the importance of wave-particle interactions.

Chorus waves contribute to the local acceleration and loss of relativistic electrons in the outer belt via wave-particle interactions (Horne and Thorne 2003; Katoh and

*Correspondence: ozaki@is.t.kanazawa-u.ac.jp

¹ Graduate School of Natural Science and Technology, Kanazawa University, Kakuma-machi, Kanazawa 920-1192, Japan

Full list of author information is available at the end of the article

Omura 2007; Kasahara et al. 2009; Thorne et al. 2013). Chorus waves in the extremely low frequency (ELF) and very low frequency (VLF) bands are the most common whistler mode waves in the inner magnetosphere (Burtis and Helliwell 1969; Tsurutani and Smith 1974). Chorus waves have a frequency range between about $0.1f_{ceq}$ and $0.7f_{ceq}$, where f_{ceq} is the equatorial electron gyrofrequency. Additionally, chorus waves usually have a frequency gap at half the equatorial electron gyrofrequency and are classified into lower ($0.1f_{ceq}$ to $0.5f_{ceq}$) and upper ($0.5f_{ceq}$ to $0.7f_{ceq}$) bands below and above the gap (Santolík et al. 2003). The gap can be caused by a nonlinear damping process (Yagitani et al. 2014). Hiss waves in the ELF band are also important for loss of relativistic electrons (Summers et al. 2008). Magnetosonic waves (sometimes referred to as equatorial noises) below the lower hybrid frequency can also contribute to local acceleration via wave–particle interactions (e.g., Horne et al. 2007). Electromagnetic ion cyclotron (EMIC) waves below the proton gyrofrequency (Jacobs et al. 1964; Fukunishi et al. 1981; Pickett et al. 2010) can contribute to loss of relativistic electrons, due to strong pitch angle scattering (Rodger et al. 2008; Jordanova et al. 2008; Miyoshi et al. 2008; Omura and Zhao 2012). These plasma waves are major candidates in the rapid local acceleration and loss processes of relativistic electrons in the radiation belts.

Brief overview of search coil magnetometers

From the dawn of space exploration to present, search coil magnetometers have contributed to understanding of the radiation belts, magnetospheric dynamics, and planetary science. The specifications of the search coil magnetometers on board the Arase satellite, which is formerly known as the Exploration of energization and Radiation in Geospace (ERG) mission, and other major satellites are listed in Table 1. Because of their high robustness under harsh (temperature and radiation) environments, search coil magnetometers have been widely used in space for over a half century, and ongoing research efforts have resulted in new techniques for achieving wider bandwidth, increased miniaturization, and improved noise equivalent magnetic induction (NEMI) values. To achieve a wider bandwidth, a new sensor that can simultaneously monitor two (a few kHz and 100 kHz) different resonant frequencies was proposed (Coillot et al. 2010; Ozaki et al. 2013). Miniaturization of sensors on board the Mercury Magnetospheric Orbiter (MMO) and the Magnetospheric Multiscale (MMS) satellites has been realized using magnetic concentrators (Coillot et al. 2010; Le Contel et al. 2016), while maintaining a reasonable NEMI value. Drastic miniaturization of preamplifiers has been achieved by using

application-specific integrated circuit (ASIC) technology (Rhouni et al. 2013; Ozaki et al. 2014, 2016).

This paper focuses, in particular, on the Magnetic Search Coil (MSC) of the Plasma Wave Experiment (PWE) (Kasahara et al. 2018) on board the Arase satellite (Miyoshi et al. 2012), which plays a central role in the plasma wave observations of magnetic field vectors in the frequency range between a few Hz to 100 kHz. The MSC consists of a three-axis search coil magnetometer with a 200-mm-long magnetic core. The MSC can provide accurate waveform data (amplitude and phase) of magnetic field components because of its robustness even in plasma and radiation environments. Because accurate phase measurements of plasma waves are essential for the analysis of wave–particle interaction processes (Fukuhara et al. 2009; Katoh et al. 2018), the MSC was designed especially for magnetic field observations of chorus, hiss, and magnetosonic waves in the frequency range from a few Hz to 100 kHz, while a fluxgate magnetometer, hereafter referred to as MGF (Matsuoka et al. 2018), is used for ULF and EMIC wave observations below a frequency of 10 Hz. Design and manufacturing for the MSC were mainly performed by Kanazawa University and NIPPI Corporation, both of which were deeply involved in developments of search coil magnetometers on board the GEOTAIL (Matsumoto et al. 1994) and the MMO (Kasaba et al. 2010) satellites. Since the mission objective of the Arase satellite is to directly observe the heart of the Earth's radiation belts, the MSC was developed specifically for use in harsh radiation environments.

MSC description

Arase satellite overview

In order to understand the dynamics of Earth's radiation belts, satellite and ground-based observations along with simulation studies are conducted (Miyoshi et al. 2012; Shiokawa 2017). As part of this effort, the Arase satellite, which is equipped with particle instruments that cover a wide energy range (10 eV to 20 MeV for electrons and 10 eV to 180 keV for ions), a DC magnetometer, and plasma wave receivers for a wide frequency range (a few Hz to 10 MHz), was launched on December 20, 2016. Information on wave-normal vectors, polarizations, and refractive indices of the plasma waves is obtained by the PWE on board the Arase satellite. The MSC belonging to the PWE is composed of a triaxial sensor (referred to as MSC-S), low-noise preamplifiers (addressed as MSC-PA), and a 5-m-long extendable mast (addressed as MAST).

Figures 1 and 2 show the spinning satellite geometry axis (SGA) coordinates represented by the symbols (X , Y , Z) and the configuration of the MSC in the $\alpha\beta\gamma$ coordinates, respectively. To mitigate the magnetic noise coming from the drive signals of the MGF, the MSC-S

Table 1 Major examples of spaceborne search coil magnetometers for plasma wave measurements

Satellite	Launch year	Core length (m)	Frequency range	NEMI
OGO-I–VI (Frandsen et al. 1969)	1964–1969	0.27	0.01 Hz to 1 kHz	≤ 100 fT/Hz ^{1/2} at 50 to 1000 Hz
IMP-8 (Gurnett et al. 1976)	1973	0.46	40 Hz to 1.78 kHz	10 fT/Hz ^{1/2} at 1 kHz
GEOS 1 and 2 (S-300 Experimenters 1979)	1977 and 1978	?	0.1 to 450 Hz	0.1 pT/Hz ^{1/2} at 30 Hz
GEOS 1 and 2 (S-300 Experimenters 1979)	1977 and 1978	?	0.45 to 20 kHz	3 fT/Hz ^{1/2} at 5 kHz
ISEE-3 (Scarf et al. 1978)	1978	0.4	17 Hz to 100 kHz	20 fT/Hz ^{1/2} at 200 Hz
DE-1 and DE-2 (Shawhan et al. 1981)	1981	0.4	1 Hz to 1 kHz	0.1 γ -Hz < 35 kHz
Akebono (Fukunishi et al. 1990)	1989	0.3	1 to 800 Hz	0.3 pT at 10 Hz
Galileo (Gurnett et al. 1992)	1989	0.26	5 Hz to 3.5 kHz	50 fT/Hz ^{1/2} at 100 Hz
Galileo (Gurnett et al. 1992)	1989	0.28	1 to 50 kHz	3 fT/Hz ^{1/2} at 20 kHz
CRRES (Anderson et al. 1992)	1990	0.4	5.6 Hz to 400 kHz	35 μ V/nT Hz up to 10 kHz
GEOTAIL (Matsumoto et al. 1994)	1992	0.3	10 Hz to 12 kHz	20 fT/Hz ^{1/2} at 100 Hz
Freja (Holback et al. 1994)	1992	0.27	30 Hz to 16 kHz	10 fT/Hz ^{1/2}
WIND (Bougeret et al. 1995)	1994	0.4	A few Hz to 3 kHz	10 fT/Hz ^{1/2} at 1 kHz
Magion 4 (Blęki et al. 1997)	1995	?	1 Hz to 2 kHz	30 fT/Hz ^{1/2} at 100 Hz
Polar (Gurnett et al. 1995)	1996	0.4	0.1 Hz to 50 kHz	10 fT/Hz ^{1/2} at 1 kHz
FAST (Elphic et al. 2001)	1996	0.18	10 Hz to 16 kHz	3 fT/bit ⁻¹ at 16 kHz
FAST (Elphic et al. 2001)	1996	0.53	10 Hz to 1 MHz	3 fT/bit ⁻¹ at 16 kHz
Interball 2 (Lefeuvre et al. 1998)	1996	?	0.01 Hz to 1 kHz	8 fT/Hz ^{1/2} at 400 Hz
Interball 2 (Lefeuvre et al. 1998)	1996	?	1 to 20 kHz	?
Interball 2 (Lefeuvre et al. 1998)	1996	?	40 kHz to 2 MHz	3 fT/Hz ^{1/2} at 100 kHz
Cassini (Gurnett et al. 2004)	1997	0.25	1 Hz to 20 kHz	20 fT/Hz ^{1/2} at 1 kHz
Cluster II (Cornilleau-Wehrlin et al. 2003)	2000	0.27	0.1 Hz to 4 kHz	10 fT/Hz ^{1/2} at 1 kHz
DEMETER (Séran and Ferreau 2005)	2004	0.17	A few Hz to 20 kHz	4 fT/Hz ^{1/2} at 6 kHz
THEMIS (Roux et al. 2008)	2007	0.17	0.1 Hz to 4 kHz	20 fT/Hz ^{1/2} at 1 kHz
Van Allen Probes (Kletzing et al. 2013)	2012	0.4	10 Hz to 12 kHz	5 fT/Hz ^{1/2} at 3 kHz
MMS (Le Contel et al. 2016)	2015	0.1	1 Hz to 6 kHz	20 fT/Hz ^{1/2} at 1 kHz
MMO (Kasaba et al. 2010)	Future	0.1	0.1 Hz to 20 kHz	50 fT/Hz ^{1/2} at 1 kHz
MMO (Coillot et al. 2010)	Future	0.1	10 to 640 kHz	8 fT/Hz ^{1/2} at 100 kHz
Arase (ERG)	2016	0.2	1 Hz to 100 kHz	20 fT/Hz ^{1/2} at 2 kHz

is mounted on the top of the MAST along the + Y axis in the SGA coordinates, while the MGF is mounted on a separate mast that extends from the other side. The α and β axes are tilted by 45° from the X and Y axes. The γ axis is parallel to the Z (spin) axis. Because of the high-radiation environment (over 100 krad), the MSC-PA is mounted on the + Y panel inside the satellite body.

A block diagram of the MSC is shown in Fig. 3. The AC magnetic field vectors below 20 kHz are digitally processed by the WaveForm Capture (WFC) for the waveform observations and the Onboard Frequency Analyzer (OFA) for the spectrum observations (Kasahara et al. 2018). Additionally, the B_γ component along the spin axis is measured by the High Frequency Analyzer (HFA) for the spectrum measurements from 10 to 100 kHz

(Kumamoto et al. 2018). The NEMI requirements for the plasma wave observations by the Arase satellite are listed in Table 2. The sensor and low-noise preamplifiers were carefully designed to satisfy those requirements.

Sensor

The one-axis sensor for the MSC-S consists of a magnetic core wound with a solenoid coil of copper wire and is equipped with an electrostatic shield to avoid electric field pickup (Ozaki et al. 2015). The insulator coating on the copper wire and coil bobbin is fabricated from radiation-hardened polyimide plastic designed for use in high-radiation environments. An RLC resonant circuit with a resistive component for causing magnetic loss is provided as an equivalent circuit of the one-axis sensor for

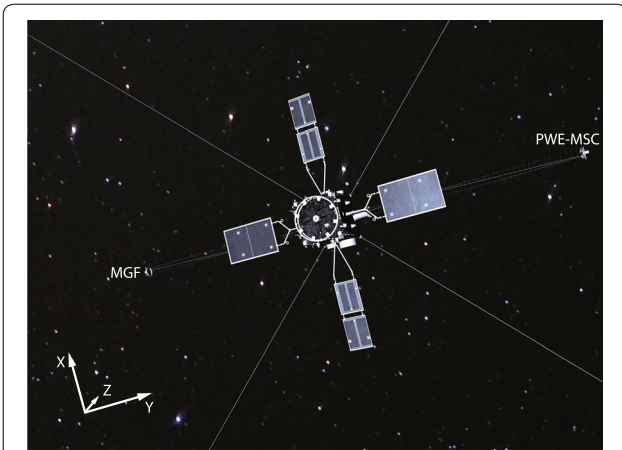


Fig. 1 Arase satellite in the SGA coordinates. The Z axis is located along the satellite spin axis. This figure is a modification of an original version produced by the ERG project

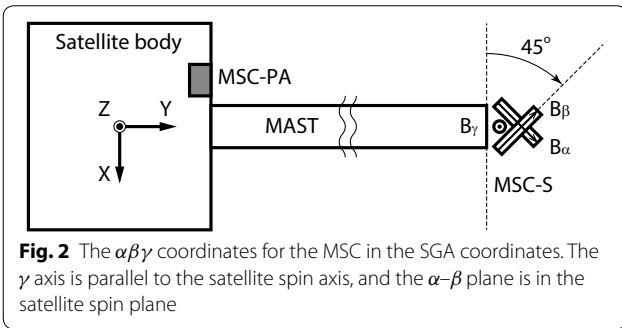


Fig. 2 The $\alpha\beta\gamma$ coordinates for the MSC in the SGA coordinates. The γ axis is parallel to the satellite spin axis, and the α - β plane is in the satellite spin plane

the MSC-S, as shown in Fig. 4. The sensor impedance Z_s at the coil terminals is expressed as

$$Z_s = \frac{R + j\omega L}{\left(1 - \omega^2 CL + \frac{R}{R_{\text{loss}}}\right) + j\omega\left(CR + \frac{L}{R_{\text{loss}}}\right)}, \quad (1)$$

where R , L , C , R_{loss} , and ω are the resistance, inductance, parasitic capacitance of the coil, resistive component for the magnetic losses, and the angular frequency, respectively. The magnitude of the sensor impedance is approximately

$$|Z_s| \approx \begin{cases} R & \left(0 < f < \frac{R}{2\pi L}\right) \\ |j\omega L| & \left(\frac{R}{2\pi L} < f < f_r\right), \\ R_{\text{loss}} & (f = f_r) \\ \left|\frac{1}{j\omega C}\right| & (f > f_r) \end{cases}, \quad (2)$$

where

$$f_r = \frac{1}{2\pi\sqrt{LC}} \quad (3)$$

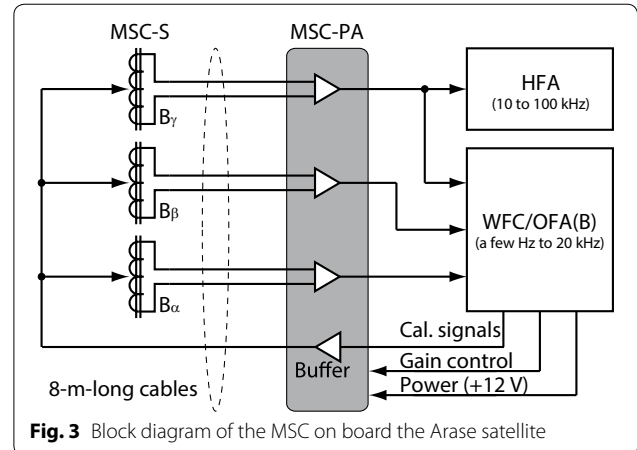


Fig. 3 Block diagram of the MSC on board the Arase satellite

Table 2 NEMI requirements for the MSC

Frequency (Hz)	NEMI ($\mu\text{T}/\text{Hz}^{1/2}$)	Measurement target
1–10	30–3	EMIC waves
30	1	Magnetosonic waves
2 k	0.2	Chorus and hiss waves

is the resonant frequency of the coil. To reduce the parasitic capacitance, the coil consists of layers wound in the same direction (Dalessandro et al. 2007). An induced voltage e is given directly from Faraday's law as

$$e = -\frac{d\Phi}{dt} \quad (4)$$

$$= -j\omega\mu_{\text{app}}NSB, \quad (5)$$

where Φ is the magnetic flux, μ_{app} is the apparent permeability of the magnetic core, N is the number of solenoid coil turns, S is the cross-sectional area of the magnetic core, and B is the ambient external magnetic field. Since a conventional magnetic core formed in a square column shape was used on the MSC on board the Arase satellite, the apparent permeability is

$$\frac{1}{\mu_{\text{app}}} = \frac{1}{\mu_i} + \left(\frac{d}{l}\right)^2 \left(\ln\left(\frac{2l}{d}\right) - 1\right) \left(1 - \frac{1}{\mu_i}\right), \quad (6)$$

where μ_i , l , and d are the initial permeability, the length, and the side length of the core, respectively (Séran and Ferreau 2005). Basic parameters of the MSC-S are listed in Table 3. The mass of the one-axis sensor for the MSC-S with a 200-mm-long core was 91 g, which is almost the same as the 100-mm-long sensor on board the MMO satellite. The mass saving for the MSC-S was realized by an optimization of magnetic wire (the number of turns and

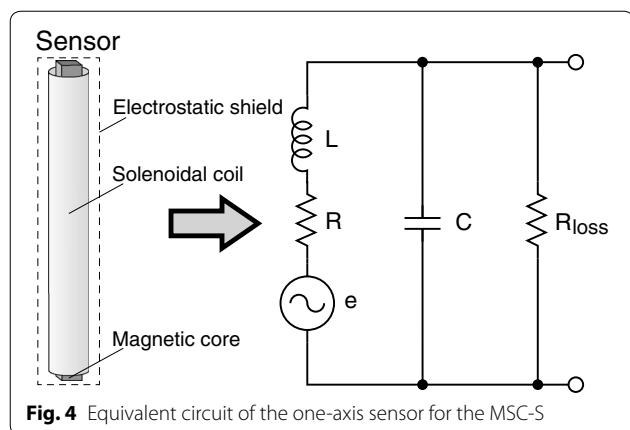


Fig. 4 Equivalent circuit of the one-axis sensor for the MSC-S

Table 3 Parameters for the MSC-S

Item	Value	Unit
Mass of the one-axis sensor	91	g
Magnetic core (permalloy)	5 × 5 × 200	mm
Apparent permeability of the magnetic core	452	
Magnetic wire diameter	0.07	mm
Number of turns for the solenoid coil	14,000	turns
Electrostatic shield	Al plate (thickness 0.2 mm) with two slits	

the diameter), which was designed such that the thermal noise levels of resistive component should be less than the noise property of preamplifier.

MAST

The three sensors of the MSC-S are orthogonally assembled on a top plate to detect magnetic field vectors. The top plate is made of carbon fiber-reinforced plastic (CFRP)/aluminum honeycomb sandwich panel (CFRP surface thickness 1.1 mm and honeycomb thickness 10 mm) to reduce the eddy current losses on the plate. A thermistor is attached on the top plate to provide the temperature of the MSC-S as housekeeping data. The MSC-S is mounted on the top of the MAST to mitigate electromagnetic noises from the satellite body. Finally, the MSC-S is covered by a multilayered insulator (MLI) to isolate it thermally from the space environment. The total mass of the MAST equipped with the MSC-S is 3.8 kg.

Figure 5a, b shows photographs of the MSC-S installed on the top of the MAST in both stowed and extended positions. In a ground test for full extension, the

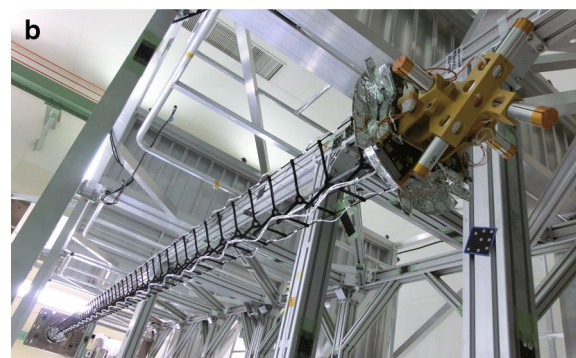


Fig. 5 Photographs of the MSC-S mounted on the top of the MAST in both **a** stowed and **b** extended positions. The length of the MAST in full extension is 5.2 m from the side panel of the satellite body

mechanical alignment accuracy of the MAST was found to be within 2° in the $\alpha\beta\gamma$ coordinates. Wave-normal and Poynting vectors can be measured with accuracy levels within a few degrees. Wave-normal and Poynting vectors, along with polarizations, are useful for determining the generation regions of plasma waves (e.g., Nagano et al. 1996; Santolík et al. 2003; Horne et al. 2007).

Preamplifier

Preamplifiers for search coil magnetometers can be classified into two types: one uses a voltage amplifier with flux feedback (e.g., Matsumoto et al. 1994), and the other uses a current amplifier with an equalizer (e.g., Ozaki et al. 2014). While most preamplifiers used in previous missions were the voltage-sensing type, the current-sensing type was adopted for the MSC-PA to reduce the wire harness between the MSC-PA installed in the satellite body and the MSC-S at the top of the MAST. When an induction coil sensor is connected to an ideal current amplifier, the parasitic capacitance between the coil terminals is virtually shorted. This allows resonance to be effectively eliminated without the flux feedback coil that is used for damping in voltage-sensing type preamplifiers.

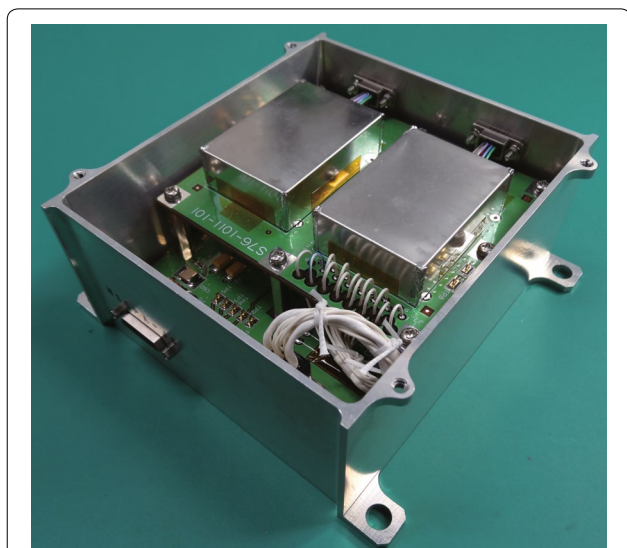


Fig. 6 Photograph of the MSC-PA. The size of chassis is 110 × 125 × 60 mm (protruding parts not included)

As a result, the harness for the flux feedback coils can be eliminated in the current-sensing type.

The MSC-PA consists of three sets of low-noise current amplifiers, equalizers, and gain adjustment amplifiers. The MSC-PA has a buffer amplifier to apply calibration signals to the sensors from the main electronics box of the PWE. The design concept behind the low-noise current amplifier and equalizer is based on the preamplifier on board the MMO satellite (Kasaba et al. 2010). The gain adjustment amplifier can select 0- or 20-dB ($\times 1$ or $\times 10$) voltage gains to prevent saturation by large-amplitude chorus waves (Cattell et al. 2008), which can reach amplitudes up to several nT. The saturation levels of low (0 dB) and high (20 dB) gain cases are 10 and 1 nT at a frequency of 1 kHz, respectively.

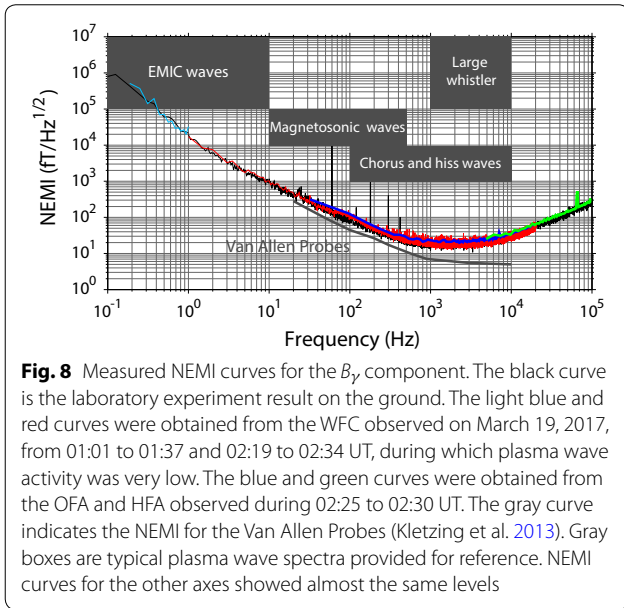
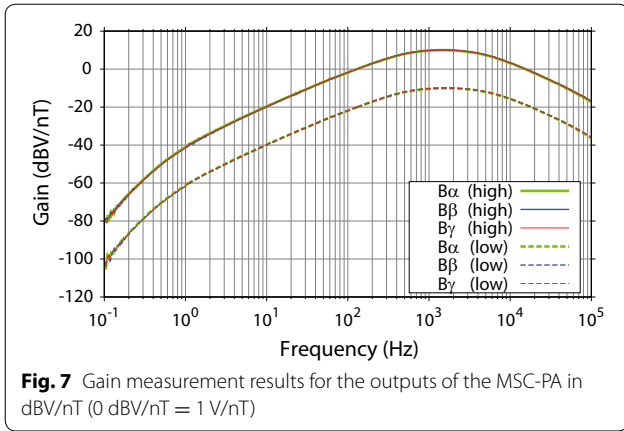
Figure 6 shows a photograph of the MSC-PA housed in aluminum chassis (side and top thickness 2 mm; bottom thickness 3 mm). The thickness was calculated to satisfy the total ionizing dose limit of 100 krad during the nominal mission life (1 year). The electrical circuits for B_α and the buffer amplifier are installed on the bottom printed circuit board (PCB) and the circuits for B_β and B_γ are installed on the top PCB. The electrical circuits for each magnetic field component are electrically protected by internal shield boxes to reduce internal crosstalk and improve radiation tolerance. The mass of the MSC-PA, including the chassis, is 0.6 kg. The nominal power consumption is 0.43 W. A heater and a thermometer for house keeping are attached to the top of the chassis.

Results and discussion

Transfer function and NEMI

The transfer function measurements of B_α , B_β , and B_γ for the low- and high-gain cases are plotted in Fig. 7. These measurements were performed using a 1-m-diameter Helmholtz coil in a magnetically shielded room at Kanazawa University. The results show a good agreement among three axes. More specifically, the difference is less than 1 dB except the lowest frequency end. The shape of the transfer function is similar to that for a search coil magnetometer using a typical voltage amplifier in the frequency domain. Because it focuses fundamentally on the measurements of chorus and hiss waves below the equatorial gyrofrequency (typically several kHz), the MSC was designed to have the resonant frequency of 2 kHz. The resonance is effectively damped by the current amplifier, and the transfer function is adjusted by the equalizer. The gain less than 1 Hz is proportional to ω^2 to avoid signal saturation caused by the background geomagnetic field at the satellite spin rate (approximately 1/8 Hz). The gain between 1 and 500 Hz is proportional to ω based on Faraday's law. The use of the current amplifier on board the Arase satellite is the first in the satellite experiments for the radiation belts.

Figure 8 shows the NEMI of the MSC for the γ component, which is least influenced by the satellite spin modulation. Here, it can be seen that the NEMI sufficiently satisfies the requirements of the Arase satellite listed in Table 2. The best NEMI is 20 fT/Hz^{1/2} at 2 kHz, which is sufficient for the observations of chorus and hiss waves. The onboard NEMI (light blue) curve was calculated as an average of 29 sets of 16-s waveform data observed on March 19, 2017, from 01:01 to 01:37 UT, during which magnetic activity was very low. The onboard NEMI (red) curve was also calculated as an average of 30 sets of 2-s waveform data during 02:19 to 02:34 UT. The NEMI can be shown up to a frequency of 20 kHz due to the anti-aliasing filter of the WFC receiver. The green and blue curves were obtained from the averaged spectra by the OFA and HFA observed during 02:25 and 02:30 UT. These NEMI curves showed quite similar levels to the ground data (black). For reference purposes, the NEMI for the Van Allen Probes (Kletzing et al. 2013) and the typical ranges of intensity and frequency of the plasma waves are also shown in Fig. 8. The difference in NEMI between the Arase satellite and the Van Allen Probes is caused by the difference in sensor length. As listed in Table 1, the core length for the Van Allen Probes is twice as long as that for the Arase satellite. A longer core yields a higher value of the apparent permeability as expected from Eq. (6). However, the NEMI differences between the Arase satellite and the Van Allen Probes have no practical impact on the observations of chorus and hiss waves.



Crosstalk and directionality

A three-dimensional simulation was performed using an electromagnetic solver (PHOTO-EDDY ω) based on the finite element method to determine an acceptable gap between each sensor. Figure 9 shows the simulation model used for the crosstalk. Note that only three magnetic cores orthogonally crossed each one-axis core with a same gap length are modeled in the simulation box, and the effects of the eddy current on conductive materials were neglected to conserve computer memory in the simulation. Nevertheless, this model is considered adequate for evaluating crosstalk because magnetic flux behavior is predominantly affected by the magnetic core. The magnetic flux for each core is computed by applying uniform magnetic field vectors along the α axis. The crosstalk value is calculated as

$$CT = 20 \log_{10} \left(\frac{\int_{\text{core}} \mathbf{B} \cdot d\mathbf{S}_\beta}{\int_{\text{core}} \mathbf{B} \cdot d\mathbf{S}_\alpha} \right) = 20 \log_{10} \left(\frac{\int_{\text{core}} \mathbf{B} \cdot d\mathbf{S}_\gamma}{\int_{\text{core}} \mathbf{B} \cdot d\mathbf{S}_\alpha} \right), \quad (7)$$

where the boldface type indicates a vector and dS is an area element for each core. To obtain accurate magnetic field vectors with a direction error less than a few degrees, the crosstalk between each component should be less than -40 dB.

Figure 10 shows the results of simulated crosstalk between the magnetic cores as a function of the gap length. The size of each one-axis core is $5 \times 5 \times 200$ mm, which is the same as that of the magnetic core for the MSC-S. The simulations were performed for three cases of magnetic permeability ($\mu_i = 1000, 2000, \text{ and } 10,000$). The crosstalk values for $\mu_i = 1000, 2000, \text{ and } 10,000$ are $-47.2, -45.7, \text{ and } -44.4$ dB for the gap of 20 mm, respectively.

The measurement results obtained using the engineering model for the MSC-S ($\mu_i = 10,000$) are added to Fig. 10 for reference to the simulation case of $\mu_i = 10,000$. The measurements were evaluated by comparing the output voltages between parallel and perpendicular arrangements for the standard magnetic field vector generated by a Helmholtz coil. Differences between the simulation and measurement results were due to inaccuracy of sensor alignment because crosstalk is sensitive to the sensor geometry. Here, the apparent permeability coefficients of the one-axis magnetic core ($5 \times 5 \times 200$ mm) for $\mu_i = 1000, 2000, \text{ and } 10,000$ are calculated as 321, 383, and 452, respectively, from Eq. (6). One interesting point is that the crosstalk ratio for the three magnetic permeability cases in the simulation is almost constant when the gap is over 15 mm. This implies that crosstalk differences for each gap are indirectly related to apparent permeability.

To confirm the relationship between the crosstalk and apparent permeability, we calculated the ratio of the crosstalk for each initial permeability and that of the apparent permeability. These ratios as a function of the gap are shown in Fig. 11. From the comparison results, we found that when the gap is over 15 mm, the crosstalk ratios between $\mu_i = 2000$ and $\mu_i = 1000$, and those between $\mu_i = 10,000$ and $\mu_i = 1000$ showed a good similarity with the ratios of the apparent permeability because the magnetic coupling between the cores decreases with the increasing gap. The crosstalk depends strongly on the apparent permeability. Finally, the MSC-S was designed with a gap length of 18 mm. Although sensor geometry is usually determined by trial and error, our understanding of this crosstalk dependence on apparent permeability

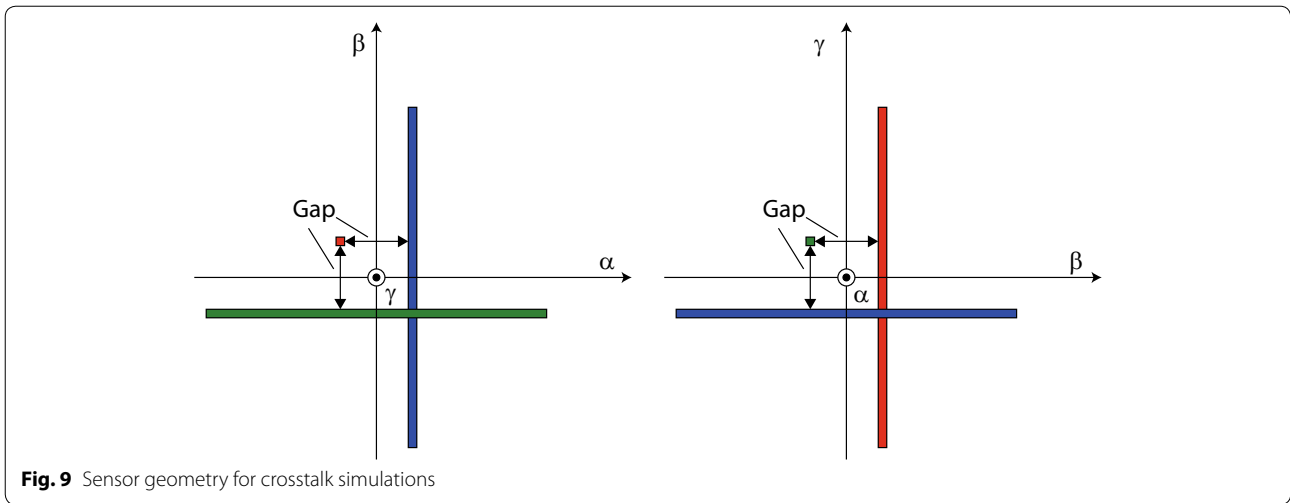


Fig. 9 Sensor geometry for crosstalk simulations

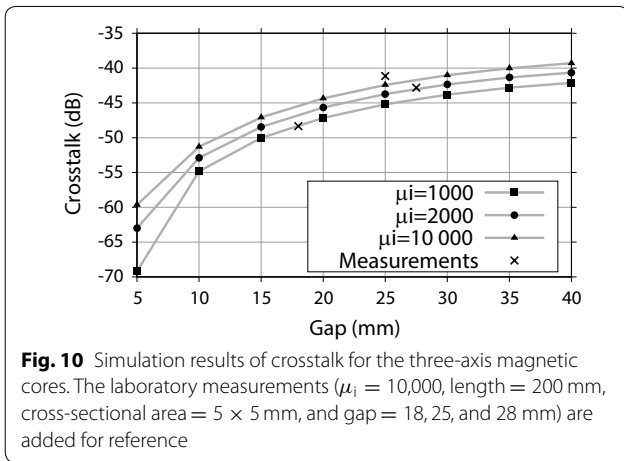


Fig. 10 Simulation results of crosstalk for the three-axis magnetic cores. The laboratory measurements ($\mu_i = 10,000$, length = 200 mm, cross-sectional area = 5×5 mm, and gap = 18, 25, and 28 mm) are added for reference

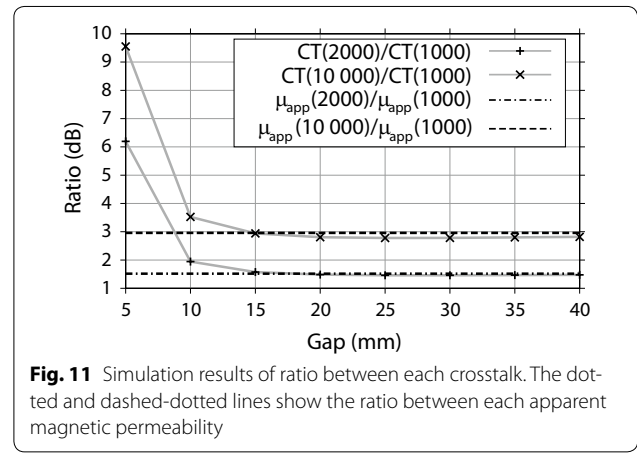


Fig. 11 Simulation results of ratio between each crosstalk. The dotted and dashed-dotted lines show the ratio between each apparent magnetic permeability

allows us to design a triaxial sensor geometry with an acceptable level of crosstalk.

Next, the measurement results of the directionality of the MSC for each gain mode are plotted in Fig. 12. These measurements are normalized by the maximum value to clearly show the null depth in unit of dB. Although directionality is usually measured by rotating a sensor emplaced on a turntable, these measurements were performed by rotating the input magnetic field vector for the MSC-S with an angular resolution of 0.5° . An arbitrary direction of a magnetic field vector was generated by using a three-axis Helmholtz coil. This had the advantage for reducing the alignment errors of the MSC-S on the turntable and achieving a higher angular resolution. All measurements show a clear null depth less than -40 dB, which is consistent with the crosstalk simulation results.

Calibration

Onboard calibration is performed to identify the validity of the transfer function of the MSC in the radiation belts. Continuous square waves, which are used as calibration signals, are supplied to the calibration coils at an arbitrary frequency through the buffer amplifier of the MSC-PA as shown in Fig. 3. The transfer function is obtained at the fundamental frequency and its harmonics. An example of an onboard calibration conducted on March 10, 2017, at 23:39 UT with 512-Hz square waves is shown in Fig. 13. The top panel shows the output waveform for the onboard calibration. The buffer amplifier consists of a low-pass filter for mitigating the effect of induction voltage (time derivative of the applied magnetic field for calibration) appearing as the discontinuity in the square pulses. When applying square pulses, the output waveform looks like a row of shark teeth. In the bottom panel, the black line indicates the laboratory experiment result and the dots denote the onboard calibration results at 512 Hz and its harmonics. The onboard

calibration output shows a good agreement with the laboratory experiment data. The use of harmonics is effective for obtaining not only the signal power, but also the phase information in a wide frequency band (Matsuda et al. 2018). Such a use of harmonics was adopted in the calibration of the search coil magnetometers on board the Time History of Events and Macroscale Interactions during Substorms (THEMIS) satellites (Roux et al. 2008).

Additionally, cross-calibration between the MSC and MGF is important for verifying the health of both instruments at frequencies less than 10 Hz. Figure 14 shows the intensity variations of geomagnetic field in the X–Y (spin) plane observed by the MSC and the MGF during 01:00 to 01:40 UT, March 19, 2017. The intensity of background geomagnetic field measured by the MSC is obtained from the satellite spin modulation component in the waveform data. Since the alignment error offsets between the MSC and the MGF were not corrected, the intensity difference between them was a few % in the spin plane. The difference is comparable to the cross-calibration results of the other missions (Robert et al. 2014). These differences can be improved by correcting the alignment errors of the MAST. Furthermore, this good agreement indicates that the MSC was not affected by Barkhausen noise, in which noise signals are generated when a suddenly changing magnetic field is applied to a magnetic core. These results indicate that the MSC can cooperate with the MGF in the background geomagnetic field observations.

Extension operation for the MAST

Figure 15 shows the magnetic field spectrum measured during the extension operation for the MAST conducted on January 17, 2017. To prevent disturbances to the

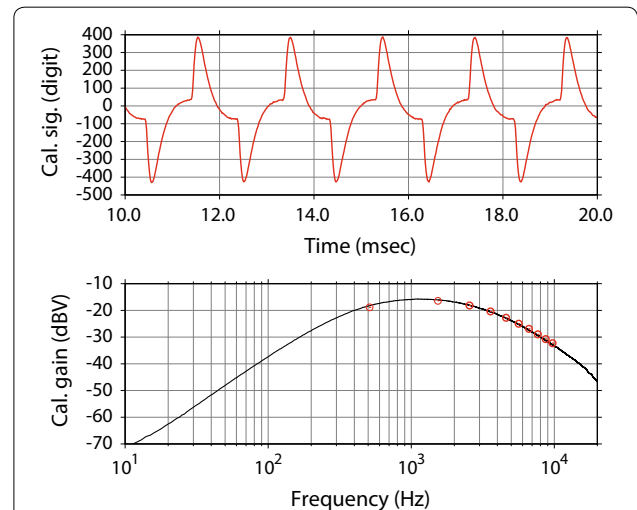


Fig. 13 Example of the onboard calibration result of the B_{γ} component. The upper panel is the waveform obtained at 23:39 UT, March 10, 2017, by the WFC for applied square pulses having a fundamental frequency of 512 Hz. The bottom panel shows the gain of the onboard calibration (dots) at the fundamental frequency and its harmonics. The black line indicates the gain measured by a laboratory experiment for reference

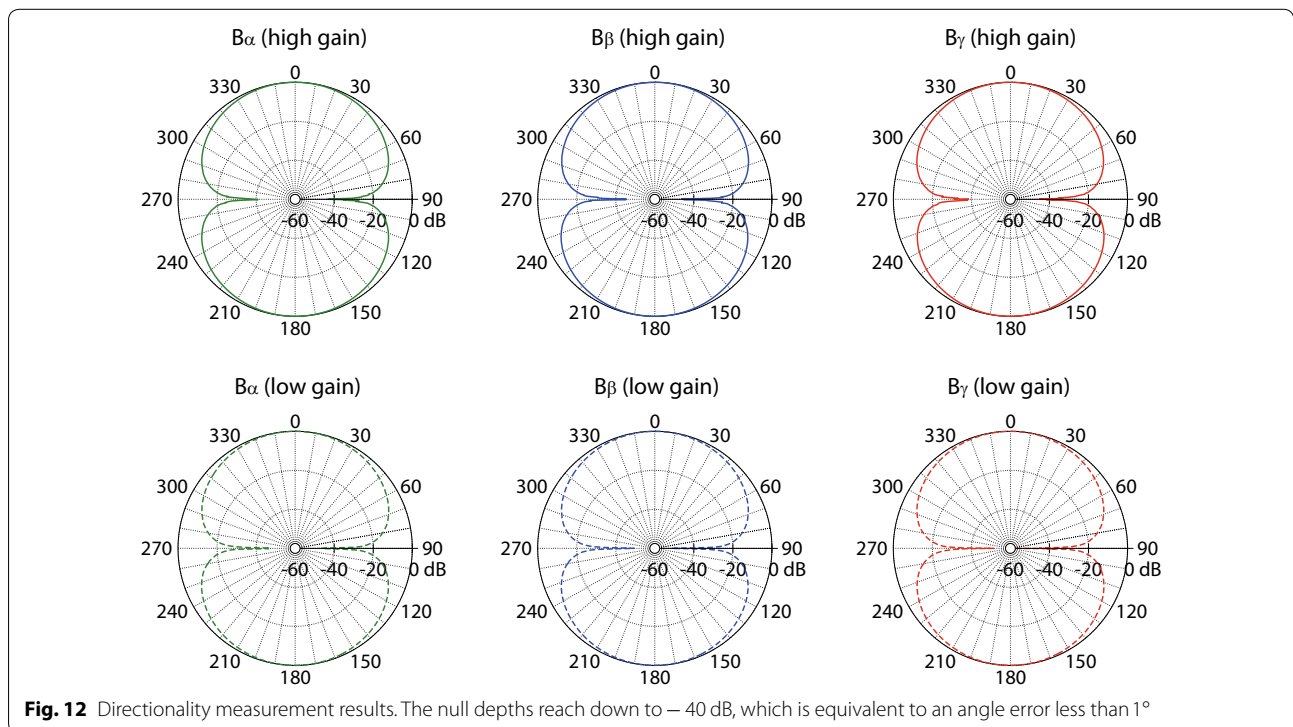


Fig. 12 Directionality measurement results. The null depths reach down to -40 dB, which is equivalent to an angle error less than 1°

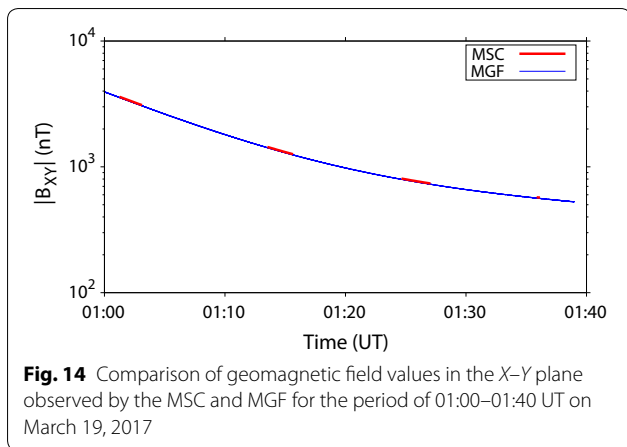


Fig. 14 Comparison of geomagnetic field values in the X-Y plane observed by the MSC and MGF for the period of 01:00–01:40 UT on March 19, 2017

satellite’s attitude, the MAST was partially extended to 0.3 m at 21:15 UT and then fully extended up to 5 m during the period from 21:37 to 21:45 UT. Noise enhancements detected at 21:15 UT and from 21:37 to 21:45 UT were caused by motor current during the extension process. Figure 16 shows the 1-min averaged intensities ($|B| = \sqrt{|B_\alpha|^2 + |B_\beta|^2 + |B_\gamma|^2}$) at 21:00 UT as a typical pre-extension intensity, at 21:30 UT for the partial extension (0.3 m), and at 21:55 UT after full extension (5 m). The averaged noise attenuation ratio below 300 Hz was 7 dB for the partial extension (0.3 m), and the magnetic field intensity was found to have decreased to the NEMI level as a result of attenuation over 25 dB after full extension (5 m). The attenuation ratios for a line current source and a small magnetic dipole are proportional to $1/r^2$ and $1/r^3$, respectively, where r is the distance between the MSC-S and a noise source. Therefore, a noise less than a few hundred Hz may be caused by a small magnetic dipole inside the satellite body. On the other hand, the averaged noise attenuation ratios around 1 kHz (800–1200 Hz) were approximately 4 dB for partial extension

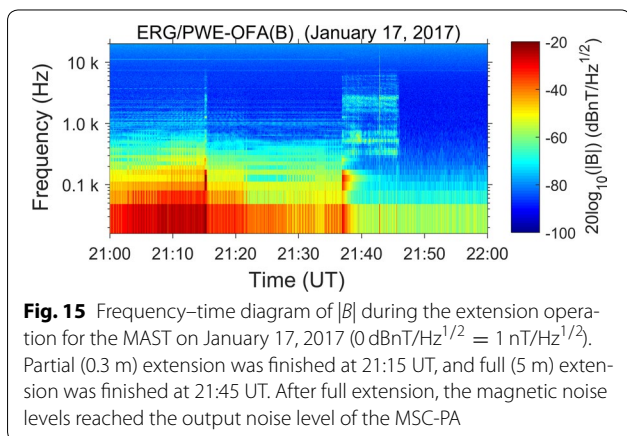


Fig. 15 Frequency–time diagram of $|B|$ during the extension operation for the MAST on January 17, 2017 ($0 \text{ dBnT/Hz}^{1/2} = 1 \text{ nT/Hz}^{1/2}$). Partial (0.3 m) extension was finished at 21:15 UT, and full (5 m) extension was finished at 21:45 UT. After full extension, the magnetic noise levels reached the output noise level of the MSC-PA

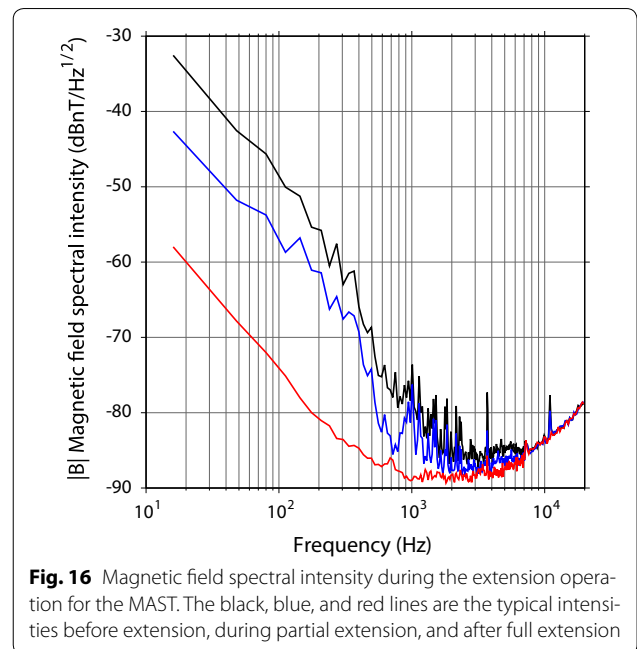


Fig. 16 Magnetic field spectral intensity during the extension operation for the MAST. The black, blue, and red lines are the typical intensities before extension, during partial extension, and after full extension

and 10 dB after full extension. The noise around 1 kHz (800–1200 Hz) would be radiated from a line source (e.g., current lines from solar paddles). Ultimately, as a result of the successful extension operation for the MAST, we are able to conduct magnetic field observations with good low-noise properties.

Initial observation result

Figure 17 shows an example of dynamic spectrum of magnetic field observed at 04:36 UT, March 21, 2017. As can be seen in the figure, clear fine structures of successive rising tone elements of chorus waves with a high signal-to-noise ratio were observed near the plasma-pause. Simultaneously, pulsating aurora was observed near the magnetic conjugate point (the Arase location was $L \approx 6.2$), Husafell, Iceland (not shown in this paper). The behavior of chorus waves is not only important for understanding radiation belt dynamics, but also for understanding the generation mechanism of pulsating aurora (Nishimura et al. 2010).

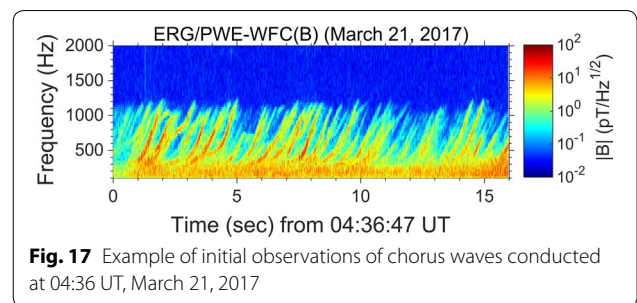


Fig. 17 Example of initial observations of chorus waves conducted at 04:36 UT, March 21, 2017

Conclusions

In this paper, the detailed performance characteristics of the MSC on board the Arase satellite were presented. The MSC was designed and developed to provide accurate magnetic field vectors when used in a high-radiation environment. The NEMI is $1 \text{ pT/Hz}^{1/2}$ at 10 Hz and $20 \text{ fT/Hz}^{1/2}$ at 2 kHz, which satisfy the scientific requirement levels of the mission. The gain has two modes to prevent saturation (10 nT for 0 dB and 1 nT for 20 dB at 1 kHz) when encountering plasma waves with an unusually large amplitude in the radiation belts. The MSC will help further understanding of the characteristics and activities of plasma waves in radiation belt dynamics.

Authors' contributions

MO developed the MSC and wrote the whole of this paper. YS designed the concept of current-sensitive preamplifier of the MSC. YK was a principal investigator of the PWE. HK and YK were co-principal investigators of the PWE. AK and FT developed the HFA receiver. SM managed the PWE data. AM was a principal investigator of the MGF and conducted the MAST extension. TS and TY manufactured the flight models of the MSC and MAST. All authors read and approved the final manuscript.

Author details

¹ Graduate School of Natural Science and Technology, Kanazawa University, Kakuma-machi, Kanazawa 920-1192, Japan. ² Research Institute for Sustainable Humanosphere, Kyoto University, Gokasho, Uji 611-0011, Japan. ³ Graduate School of Science, Tohoku University, Aoba, Sendai 980-8578, Japan. ⁴ Institute for Space–Earth Environmental Research, Nagoya University, Chikusa-ku, Nagoya 464-8601, Japan. ⁵ Institute of Space and Astronautical Science, Yoshinodai, Sagamihara 252-5210, Japan. ⁶ Aerospace Division, NIPPI Corporation, 3175 Showa-machi, Kanazawa-ku, Yokohama 236-8540, Japan.

Acknowledgements

This study was supported by a Grant-in-Aid for Young researchers from the Hokuriku Bank, Ltd. A part of this study was carried out under the joint research program of the Solar-Terrestrial Environment Laboratory, Nagoya University, and by the Japan Society for the Promotion of Science (JSPS) KAKENHI Grant Number 16H04056. The authors would like to extend sincere thanks to Mr. T. Kitase, Mr. A. Asano, and Mr. Y. Tokunaga for their efforts in the laboratory experiments and magnetic field simulations. Gratitude is also extended to Mr. H. Tanakano of the Meiwa System and Mr. Y. Sato for developing the breadboard model of the MSC, and to Dr. S. Nakazawa and Dr. M. Mita of the ISAS/JAXA for their support during the electromagnetic compatibility tests. The authors would also like to thank Dr. I. Nagano, Dr. G. Chanteur, and Dr. C. Coillot for their valuable discussions on the MSC, the NIPPI corp. members involved in the MSC, and the Mitsubishi Heavy Industries, Ltd. and Meisei Electric Co., Ltd. engineers that participated in developing the PWE. Finally, the authors would like to thank all members of the ERG project and the ERG Science Center.

Competing interests

The authors declare that they have no competing interests.

Availability of data and materials

The PWE and MGF data will be available through the ERG Science Center operated by ISAS/JAXA and ISEE/Nagoya University.

Ethics approval and consent to participate

Not applicable.

Publisher's Note

Springer Nature remains neutral with regard to jurisdictional claims in published maps and institutional affiliations.

Received: 22 August 2017 Accepted: 14 April 2018

Published online: 04 May 2018

References

- Anderson RR, Gurnett DA, Odem DL (1992) CRRES plasma wave experiment. *J Spacecr Rockets* 29:570–573
- Baker DN, Blake JB, Klebesadel RW, Higbie PR (1986) Highly relativistic electrons in the Earth's outer magnetosphere: 1. Lifetimes and temporal history 1979–1984. *J Geophys Res* 91:4265–4276. <https://doi.org/10.1029/JA091iA04p04265>
- Baker DN, Kanekal SG, Hoxie VC, Henderson MG, Li X, Spence HE, Elkington SR, Friedel RHW, Goldstein J, Hudson MK, Reeves GD, Thorne RM, Kletzing CA, Claudepierre SG (2013) A long-lived relativistic electron storage ring embedded in Earth's outer Van Allen belt. *Science* 340:186–190. <https://doi.org/10.1126/science.1233518>
- Bougeret J-L, Kaiser ML, Kellogg PJ, Manning R, Goetz K, Monson SJ, Monge N, Friel L, Meetre CA, Perche C, Sitruk L, Hoang S (1995) WAVES: the radio and plasma wave investigation on the wind spacecraft. *Space Sci Rev* 71:231–263
- Błęki J, Gadowski S, Juchniewicz J, Korepanov V, Krawczyk Z, Savin S, Słomiński J, Triska P, Vojta J, Wronowski R (1997) SAS wave experiment on board Magion 4. *Ann Geophys* 15:528–532
- Burtis WJ, Helliwell RA (1969) Banded chorus—a new type of VLF radiation observed in the magnetosphere by OGO 1 and OGO 3. *J Geophys Res* 74:3002–3010. <https://doi.org/10.1029/JA074i011p03002>
- Cattell C, Wygant JR, Goetz K, Kersten K, Kellogg PJ, von Roseninge T, Bale SD, Roth I, Temerin M, Hudson MK, Mewaldt RA, Wiedenbeck M, Maksimovic M, Ergun R, Acuna M, Russell CT (2008) Discovery of very large amplitude whistler-mode waves in Earth's radiation belts. *Geophys Res Lett* 35:L01105. <https://doi.org/10.1029/2007GL032009>
- Coillot C, Moutoussamy J, Lebourgeois R, Ruocco S, Chanteur G (2010) Principle and performance of a dual-band search coil magnetometer: a new instrument to investigate fluctuating magnetic fields in space. *IEEE Sens J* 10:255–260
- Cornilleau-Wehrin N, Chanteur G, Perraut S, Rezeau L, Robert P, Roux A, De Villedary C, Canu P, Maksimovic M, De Conchy Y, Hubert D, Lacombe C, Lefeuvre F, Parrot M, Pinçon JL, Décréau PME, Harvey CC, Louarn Ph, Santolik O, Alleyne H, St C, Roth M, Chust T, Le Contel O (2003) First results obtained by the Cluster STAFF experiment. *Ann Geophys* 21:437–456
- Dalessandro L, da Silveira Cavalcante F, Kolar JW (2007) Self-capacitance of high-voltage transformers. *IEEE Power Electron* 22:2081–2092
- Elkington SR, Hudson MK, Chan AA (1999) Acceleration of relativistic electrons via drift-resonant interaction with toroidal-mode Pc-5 ULF oscillations. *Geophys Res Lett* 26:3273–3276. <https://doi.org/10.1029/1999GL003659>
- Elphic RC, Means JD, Snare RC, Strangeway RJ, Kepko L, Ergun RE (2001) Magnetic field instruments for the fast auroral snapshot explorer. *Space Sci Rev* 98:151–168
- Frandsen AMA, Holzer RE, Smith EJ (1969) OGO search coil magnetometer experiments. *IEEE Trans Geosci Electron* 7:61–74
- Fukuhara H, Kojima H, Ueda Y, Omura Y, Katoh Y, Yamakawa H (2009) A new instrument for the study of wave–particle interactions in space: one-chip wave–particle interaction analyzer. *Earth Planets Space* 61:765–778. <https://doi.org/10.1186/BF03353183>
- Fukunishi H, Toya T, Koike K, Kuwashima M, Kawamura M (1981) Classification of hydromagnetic emissions based on frequency–time spectra. *J Geophys Res* 86:9029–9039. <https://doi.org/10.1029/JA086iA11p09029>
- Fukunishi H, Fujii R, Kokubun S, Hayashi K, Tohyama T, Tonegawa Y, Okano S, Sugiura M, Yumoto K, Aoyama I, Sakurai T, Saito T, Iijima T, Nishida A, Natori M (1990) Magnetic field observations on the Akebono (EXOS-D) satellite. *J Geomagn Geoelectr* 42:385–409
- Gurnett DA, Frank LA, Lepping RP (1976) Plasma waves in the distant magnetotail. *J Geophys Res* 81:6059–6071. <https://doi.org/10.1029/JA081i034p06059>
- Gurnett DA, Kurth WS, Shaw RR, Roux A, Gendrin R, Kennel CF, Scarf FL, Shawhan SD (1992) The Galileo plasma wave investigation. *Space Sci Rev* 60:341–355

- Gurnett DA, Persoon AM, Randall RF, Odem DL, Remington SL, Averkamp TF, Debowler MM, Hospodarsky GB, Huff RL, Kirchner DL, Mitchell MA, Pham BT, Phillips JR, Schintler WJ, Sheyko P, Tomash DR (1995) The POLAR plasma wave instrument. *Space Sci Rev* 71:597–622
- Gurnett DA, Kurth WS, Kirchner DL, Hospodarsky GB, Averkamp TF, Zarka P, Lecacheux A, Manning R, Roux A, Canu P, Cornilleau-Wehrin N, Galopeau P, Meyer A, Boström R, Gustafsson G, Wahlund J-E, Åhlen L, Rucker HO, Ladreiter HP, Macher W, Woollicroft LJC, Alleyne H, Kaiser ML, Desch MD, Farrell WM, Harvey CC, Louarn P, Kellogg PJ, Goetz K, Pedersen A (2004) The Cassini radio and plasma wave investigation. *Space Sci Rev* 114:395–463
- Holback B, Jansson S-E, Åhlén L, Lundgren G, Lyngdal L, Powell S, Meyer A (1994) The Freja wave and plasma density experiment. *Space Sci Rev* 70:577–592
- Horne RB, Thorne RM (2003) Relativistic electron acceleration and precipitation during resonant interactions with whistler-mode chorus. *Geophys Res Lett* 30:1527. <https://doi.org/10.1029/2003GL016973>
- Horne RB, Thorne RM, Glauert SA, Meredith NP, Pokhotelov D, Santolík O (2007) Electron acceleration in the Van Allen radiation belts by fast magnetosonic waves. *Geophys Res Lett* 34:L17107. <https://doi.org/10.1029/2007GL030267>
- Hudson MK, Elkington SR, Lyon JG, Goodrich CC (2000) Increase in relativistic electron flux in the inner magnetosphere: ULF wave mode structure. *Adv Space Res* 25:2327–2337
- Jacobs JA, Kato Y, Matsushita S, Troitskaya VA (1964) Classification of geomagnetic micropulsations. *J Geophys Res* 69:180–181. <https://doi.org/10.1029/JZ069i001p00180>
- Jordanova VK, Albert J, Miyoshi Y (2008) Relativistic electron precipitation by EMIC waves from self-consistent global simulations. *J Geophys Res* 113:A00A10. <https://doi.org/10.1029/2008JA013239>
- Kasaba Y, Bougeret J-L, Blomberg LG, Kojima H, Yagitani S, Moncuquet M, Trotignon J-G, Chanteur G, Kumamoto A, Kasahara Y, Lichtenberger J, Omura Y, Ishisaka K, Matsumoto H (2010) The plasma wave investigation (PWI) onboard the BepiColombo/MMO: first measurement of electric fields, electromagnetic waves, and radio waves around Mercury. *Planet Space Sci* 58:238–278
- Kasahara Y, Miyoshi Y, Omura Y, Verkhoglyadova OP, Nagano I, Kimura I, Tsurutani BT (2009) Simultaneous satellite observations of VLF chorus, hot and relativistic electrons in a magnetic storm “recovery” phase. *Geophys Res Lett* 36:L01106. <https://doi.org/10.1029/2008GL036454>
- Kasahara Y, Kasaba Y, Kojima H, Yagitani S, Ishisaka K, Kumamoto A, Tsuchiya F, Ozaki M, Matsuda S, Imachi T, Miyoshi Y, Hikishima M, Katoh Y, Ota M, Shoji M, Matsuoka A, Shinohara I (2018) The Plasma Wave Experiment (PWE) on board the Arase (ERG) satellite. *Earth Planets Space*. <https://doi.org/10.1186/s40623-018-0842-4>
- Katoh Y, Omura Y (2007) Relativistic particle acceleration in the process of whistler-mode chorus wave generation. *Geophys Res Lett* 34:L13102. <https://doi.org/10.1029/2007GL029758>
- Katoh Y, Kojima H, Hikishima M, Takashima T, Asamura K, Miyoshi Y, Kasahara Y, Kasahara S, Mitani T, Higashino N, Matsuoka A, Ozaki M, Yagitani S, Yokota S, Matsuda S, Kitahara M, Shinohara I (2018) Software-type Wave-Particle Interaction Analyzer on board the Arase satellite. *Earth Planets Space* 70:4. <https://doi.org/10.1186/s40623-017-0771-7>
- Kletzing CA, Kurth WS, Acuna M, MacDowall RJ, Torbert RB, Averkamp T, Bodet D, Bounds SR, Chutter M, Connerney J, Crawford D, Dolan JS, Dvorsky R, Hospodarsky GB, Howard J, Jordanova V, Johnson RA, Kirchner DL, Mokrzycki B, Needell G, Odom J, Mark D, Pfaff R Jr, Phillips JR, Piker CW, Remington SL, Rowland D, Santolík O, Schnurr R, Sheppard D, Smith CW, Thorne RM, Tyler J (2013) The electric and magnetic field instrument suite and integrated science (EMFISIS) on RBSP. *Space Sci Rev* 179:127–181
- Kumamoto A, Tsuchiya F, Kasahara Y, Kasaba Y, Kojima H, Yagitani S, Ishisaka K, Imachi T, Ozaki M, Matsuda S, Shoji M, Matsuoka A, Katoh Y, Miyoshi Y, Obara T (2018) High Frequency Analyzer (HFA) of Plasma Wave Experiment (PWE) onboard the Arase spacecraft. *Earth Planets Space*. <https://doi.org/10.1186/s40623-018-0854-0>
- Le Contel O, Leroy P, Roux A, Coillot C, Alison D, Bouabdellah A, Mirioni L, Meslier L, Galic A, Vassal MC, Torbert RB, Needell J, Rau D, Dors I, Ergun RE, Westfall J, Summers D, Wallace J, Magnes W, Valavanoglou A, Olsson G, Chutter M, Macri J, Myers S, Turco S, Nolin J, Bodet D, Rowe K, Tanguy M, de la Porte B (2016) The search-coil magnetometer for MMS. *Space Sci Rev* 199:257–282
- Lefevre F, Parrot M, Rauch JL, Poirier B, Masson A, Mogilevsky M (1998) Preliminary results from the MEMO multicomponent measurements of waves on-board INTERBALL 2. *Ann Geophys* 16:1117–1136
- Matsuda S, Kasahara Y, Kojima H, Kasaba Y, Yagitani S, Ozaki M, Imachi T, Ishisaka K, Kumamoto A, Tsuchiya F, Ota M, Kurita S, Miyoshi Y, Hikishima M, Matsuoka A, Shinohara I (2018) Onboard software of Plasma Wave Experiment aboard Arase: instrument management and signal processing of WaveForm Capture/Onboard Frequency Analyzer. *Earth Planets Space*. <https://doi.org/10.1186/s40623-018-0838-0>
- Matsumoto H, Nagano I, Anderson RR, Kojima H, Hashimoto K, Tsutsui M, Okada T, Kimura I, Omura Y, Okada M (1994) Plasma wave observations with GEOTAIL spacecraft. *J Geomagn Geoelectr* 46:59–95
- Matsuoka A, Teramoto M, Nomura R, Nose M, Fujimoto A, Tanaka Y, Shinohara M, Nagatsuma T, Shiokawa K, Obana Y, Miyoshi Y, Mita M, Takashima T, Shinohara I (2018) The ARASE (ERG) magnetic field investigation. *Earth Planets Space* 70:43. <https://doi.org/10.1186/s40623-018-0800-1>
- Miyoshi Y, Kataoka R (2005) Ring current ions and radiation belt electrons during geomagnetic storms driven by coronal mass ejections and corotating interaction regions. *Geophys Res Lett* 32:L21105. <https://doi.org/10.1029/2005GL024590>
- Miyoshi Y, Sakaguchi K, Shiokawa K, Evans D, Albert J, Connors M, Jordanova V (2008) Precipitation of radiation belt electrons by EMIC waves, observed from ground and space. *Geophys Res Lett* 35:L23101. <https://doi.org/10.1029/2008GL035727>
- Miyoshi Y, Ono T, Takashima T, Asamura K, Hirahara M, Kasaba Y, Matsuoka A, Kojima H, Shiokawa K, Seki K, Fujimoto M, Nagatsuma T, Cheng CZ, Kazama Y, Kasahara S, Mitani T, Matsumoto H, Higashino N, Kumamoto A, Yagitani S, Kasahara Y, Ishisaka K, Blomberg L, Fujimoto A, Katoh Y, Ebihara Y, Omura Y, Nosé M, Hori T, Miyashita Y, Tanaka Y-M, Segawa TT (2012) The Energization and Radiation in Geospace (ERG) Project. In: Summers D, Mann IR, Baker DN, Schulz M (eds) Dynamics of the Earth's radiation belts and inner magnetosphere. American Geophysical Union, Washington. <https://doi.org/10.1029/2012GM001304>
- Nagano I, Yagitani S, Kojima H, Matsumoto H (1996) Analysis of wave normal and pointing vectors of the chorus emissions observed by GEOTAIL. *J Geomagn Geoelectr* 48:299–307
- Nishimura Y, Bortnik J, Li W, Thorne RM, Lyons LR, Angelopoulos V, Mende SB, Bonnell JW, Le Contel O, Cully C, Ergun R, Auster U (2010) Identifying the driver of pulsating aurora. *Science* 330:81–84. <https://doi.org/10.1126/science.1193186>
- Omura Y, Zhao Q (2012) Nonlinear pitch angle scattering of relativistic electrons by EMIC waves in the inner magnetosphere. *J Geophys Res* 117:A08227. <https://doi.org/10.1029/2012JA017943>
- Ozaki M, Yagitani S, Takahashi K, Nagano I (2013) Dual-resonant search coil for natural electromagnetic waves in the near-Earth environment. *IEEE Sens J* 13:644–650
- Ozaki M, Yagitani S, Kojima H, Takahashi K, Kitagawa A (2014) Current-sensitive CMOS preamplifier for investigating space plasma waves by magnetic search coils. *IEEE Sens J* 14:421–429
- Ozaki M, Yagitani S, Takahashi K, Imacih T, Koji H, Higashi R (2015) Equivalent circuit model for the electric field sensitivity of a magnetic search coil of space plasma. *IEEE Sens J* 15:1680–1689
- Ozaki M, Yagitani S, Kojima H, Takahashi K, Koji H, Zushi T, Tokunaga Y (2016) Development of an ASIC preamplifier for electromagnetic sensor probes for monitoring space electromagnetic environments. *Earth Planets Space* 68:91. <https://doi.org/10.1186/s40623-016-0470-9>
- Pickett JS, Grison B, Omura Y, Engebretson MJ, Dandouras I, Masson A, Adrian ML, Santolík O, Décreau PME, Cornilleau-Wehrin N, Constantinescu D (2010) Cluster observations of EMIC triggered emissions in association with Pc1 waves near Earth's plasmapause. *Geophys Res Lett* 37:L09104. <https://doi.org/10.1029/2010GL042648>
- Reeves GD, McAdams KL, Friedel RHW, O'Brien TP (2003) Acceleration and loss of relativistic electrons during geomagnetic storms. *Geophys Res Lett* 30:1529. <https://doi.org/10.1029/2002GL016513>
- Reeves GD, Spence HE, Henderson MG, Morley SK, Friedel RHW, Funsten HO, Baker DN, Kanekal SG, Blake JB, Fennell JF, Claudepierre SG, Thorne RM, Turner DL, Kletzing CA, Kurth WS, Larsen BA, Niehof JT (2013) Electron acceleration in the heart of the Van Allen radiation belts. *Science* 341:991–994. <https://doi.org/10.1126/science.1237743>

- Rhouni A, Sou G, Leroy P, Coillot C (2013) Very low 1/f noise and radiation-hardened CMOS preamplifier for high-sensitivity search coil magnetometers. *IEEE Sens J* 13:159–166
- Robert P, Cornilleau-Wehrin N, Piberne R, de Conchy Y, Lacombe C, Bouzid V, Grison B, Alison D, Canu P (2014) CLUSTER-STAFF search coil magnetometer calibration—comparisons with FGM. *Geosci Instrum Methods Data Syst* 3:153–177
- Rodger CJ, Raita T, Clilverd MA, Seppälä A, Dietrich S, Thomson NR, Ulich T (2008) Observations of relativistic electron precipitation from the radiation belts driven by EMIC waves. *Geophys Res Lett* 35:L16106. <https://doi.org/10.1029/2008GL034804>
- Roux A, Le Contel O, Coillot C, Bouabdellah A, de la Porte B, Alison D, Ruocco S, Vassal MC (2008) The search coil magnetometer for THEMIS. *Space Sci Rev* 141:265–275
- Experimenters S (1979) Measurements of electric and magnetic wave fields and of cold plasma parameters on-board GEOS-1. Preliminary results. *Planet Space Sci* 27:317–339
- Santolik O, Gurnett DA, Pickett JS, Parrot M, Cornilleau-Wehrin N (2003) Spatio-temporal structure of storm-time chorus. *J Geophys Res* 108:1278. <https://doi.org/10.1029/2002JA009791>
- Scarf FL, Fredricks RW, Gurnett DA, Smith EJ (1978) The ISEE-C plasma wave investigation. *IEEE Trans Geosci Electron* 16:191–195
- Schulz M, Lanzerotti LJ (1974) Particle diffusion in the radiation belts. Springer, New York
- Séran HC, Fergeau P (2005) An optimized low-frequency three-axis search coil magnetometer for space research. *Rev Sci Instrum* 76:044502. <https://doi.org/10.1063/1.1884026>
- Shawhan SD, Gurnett DA, Odem DL, Helliwell RA, Park CG (1981) The plasma wave and quasi-static electric field instrument (PWI) for Dynamics Explorer-A. *Space Sci Instrum* 5:535–550
- Shiokawa K et al (2017) Ground-based instruments of the PWING project to investigate dynamics of the inner magnetosphere at subauroral latitudes as a part of the ERG-ground coordinated observation network. *Earth Planets Space* 69:160. <https://doi.org/10.1186/s40623-017-0745-9>
- Shprits YY, Elkington SR, Meredith NP, Subbotin DA (2008) Review of modeling of losses and sources of relativistic electrons in the outer radiation belt I: radial transport. *J Atmos Sol Terr Phys* 70:1679–1693
- Shprits YY, Subbotin D, Drozdov A, Usanova ME, Kellerman A, Orlova K, Baker DN, Turner DL, Kim KC (2013) Unusual stable trapping of the ultrarelativistic electrons in the Van Allen radiation belts. *Nat Phys* 9:699–703. <https://doi.org/10.1038/nphys2760>
- Summers D, Thorne RM, Xiao F (1998) Relativistic theory of wave-particle resonant diffusion with application to electron acceleration in the magnetosphere. *J Geophys Res* 103:20487–20500. <https://doi.org/10.1029/98JA01740>
- Summers D, Ni B, Meredith NP, Horne RB, Thorne RM, Moldwin MB, Anderson RR (2008) Electron scattering by whistler-mode ELF hiss in plasmaspheric plumes. *J Geophys Res* 113:A04219. <https://doi.org/10.1029/2007JA012678>
- Thorne RM (2010) Radiation belt dynamics: the importance of wave-particle interactions. *Geophys Res Lett* 37:L22107. <https://doi.org/10.1029/2010GL044990>
- Thorne RM, Li W, Ni B, Ma Q, Bortnik J, Chen L, Baker DN, Spence HE, Reeves GD, Henderson MG, Kletzing CA, Kurth WS, Hospodarsky GB, Blake JB, Fennell JF, Claudepierre SG, Kanekal SG (2013) Rapid local acceleration of relativistic radiation-belt electrons by magnetospheric chorus. *Nature* 504:411–414. <https://doi.org/10.1038/nature12889>
- Tsurutani BT, Smith EJ (1974) Postmidnight chorus: a substorm phenomenon. *J Geophys Res* 79:118–127. <https://doi.org/10.1029/JA079i001p00118>
- Yagitani S, Habagishi T, Omura Y (2014) Geotail observation of upper band and lower band chorus elements in the outer magnetosphere. *J Geophys Res Space Phys* 119:4694–4705. <https://doi.org/10.1002/2013JA019678>

Submit your manuscript to a SpringerOpen[®] journal and benefit from:

- Convenient online submission
- Rigorous peer review
- Open access: articles freely available online
- High visibility within the field
- Retaining the copyright to your article

Submit your next manuscript at ► springeropen.com
